Synthesis and Characterization of New $AA'BWO_6$ Perovskites Exhibiting Simultaneous Ordering of *A*-Site and *B*-Site Cations

Graham King,[†] Srinivasa Thimmaiah,[‡] Akansha Dwivedi,[†] and Patrick M. Woodward*,[†]

Department of Chemistry, The Ohio State University, 100 West 18th Avenue, Columbus, Ohio 43210-1185, and Materials Department, University of California, Santa Barbara, California 93106

Received June 22, 2007. Revised Manuscript Received September 27, 2007

Six new $AA'BB'O_6$ perovskites $KLaMnWO_6$, $NaLaMnWO_6$, $NaNdMnWO_6$, $NaTbMnWO_6$, $NaNdCoWO_6$, and $NaNdMgWO_6$ have been prepared. Each possesses the unusual combination of layered ordering of the *A*-site cations and rock-salt ordering of the *B*-site cations. The structure and properties of these samples have been characterized using monochromatic X-ray and neutron powder diffraction, UV–vis diffuse reflectance spectroscopy, and SQUID magnetometry. $NaLaMnWO_6$, $NaNdMnWO_6$, and $NaTbMnWO_6$ adopt a structure with monoclinic $P2_1$ symmetry arising from the combination of cation ordering and $a^-a^-c^+$ octahedral tilting. The structures of the other three compounds are similar, but the presence of satellite reflections in the neutron diffraction data suggests a more complicated superstructure. Each of the four $AA'MnWO_6$ samples shows a paramagnetic to antiferromagnetic transition with Néel temperatures ranging from 6 to 15 K. The $NaTbMnWO_6$ compound shows a second magnetic transition at ~9 K. The origin of two magnetic phase transitions appears to arise from coupling between the Mn^{2+} sublattice and the Tb^{3+} sublattice.

Introduction

Perovskites and perovskite-related materials are undeniably one of the most interesting classes of inorganic functional materials. Perovskites exist with properties as diverse as ferroelectricity, piezoelectricity, ferromagnetism, superconductivity, half-metallic transport, colossal magnetoresistance, and ionic conductivity. The aristotype structure is cubic with stoichiometry ABX_3. This well-known structure can be described as a three-dimensional framework of corner-sharing BX_6 octahedra with the larger *A*-site cations occupying the 12-coordinate cuboctahedral cavities within this framework. Substitution of multiple cations onto the *A*- or *B*-sites expands the compositional space that can be explored. Substitutions can alter both the properties and the symmetry. When the *B*-site cation is substituted in a 50:50 ratio to give a stoichiometry of $A_2BB'O_6$, there is a strong propensity for long-range ordering of *B* and *B'* cations in a rock-salt fashion. This type of ordering is common and has been studied extensively.[1,2]

Ordering of *A*-site cations, when it occurs, shows a strong preference for a layered arrangement. While layered ordering of *A*-site cations is common in oxygen-deficient perovskites, such as $BaLaMn_2O_5$[3] and $BaHoFe_2O_5$,[4] and *A*-site-deficient perovskites, such as $La_{1/3}NbO_3$[5] and $La_{2/3-x}Li_{3x}TiO_3$,[6,7] it is quite rare in stoichiometric perovskites.[8] The first known example was reported in 1984, when $NaLaMgWO_6$ was reported to possess both rock-salt ordering of *B*-site cations and a layered ordering of the *A*-site cations.[9] Subsequently, $KLaMgTeO_6$,[10] $NaLaMgTeO_6$,[10] $KLaMgWO_6$,[11] $NaLaMg_{2/3}Nb_{4/3}O_6$,[12] $NaLaCoWO_6$,[13] $NaLaNiWO_6$,[13] and $NaLaScNbO_6$[14] have been synthesized and reported to adopt similar structures. It is interesting to note that layered ordering of *A*-site cations is not generally observed in stoichiometric perovskites in the absence of rock-salt ordering of *B*-site cations. For example, $NaLaTi_2O_6$ does not exhibit long-range order of Na^+ and La^{3+} ions.[15]

Although a handful of $AA'BB'O_6$ perovskites with simultaneous *A*- and *B*-site cation ordering have been discovered, there is relatively little detailed structural information available on these compounds. Therefore, it was not until recently when the structure of $NaLaMgWO_6$ was reported for the first time that the link between layered ordering of *A*-site cations and bonding within the *B*-site cation sublattice was under-

* Corresponding author: e-mail woodward@chemistry.ohio-state.edu; phone 1-614-688-8274; Fax 1-614-292-0368.
[†] The Ohio State University.
[‡] University of California, Santa Barbara.

(1) Anderson, M. T.; Greenwood, K. B.; Taylor, G. A.; Poppelmeier, K. R. *Prog. Solid State Chem.* **1993**, *22*, 197.
(2) Lufaso, M. W.; Barnes, P. W.; Woodward, P. M. *Acta Crystallogr., Sect. B: Struct. Sci.* **2006**, *62*, 397.
(3) Millange, F.; Caignaert, B.; Domenges, B.; Raveau, B. *Chem. Mater.* **1998**, *10*, 1974.
(4) Woodward, P. M.; Suard, E.; Karen, P. *J. Am. Chem. Soc.* **2003**, *125*, 8889.
(5) Kennedy, B. J.; Howard, C. T.; Kubota, Y.; Kato, K. *J. Solid State Chem.* **2004**, *177*, 4552.
(6) Stramare, S.; Thangadurai, V.; Weppner, W. *Chem. Mater.* **2003**, *15*, 3974.
(7) Garcia-Martin, S.; Alario-Franco, M. A.; Ehrenberg, H.; Rodriguez-Carvajal; Amador, U. *J. Am. Chem. Soc.* **2004**, *15*, 3974.
(8) Davies, P. K. *Curr. Opin. Solid State Mater. Sci.* **1999**, *4*, 467.
(9) Sekiya, T.; Yamamoto, T.; Torii, Y. *Bull. Chem. Soc. Jpn.* **1984**, *57*, 1859.
(10) Lopez, M. L.; Veiga, M. L.; Pico, C. *J. Mater. Chem.* **1994**, *4*, 547.
(11) Arillo, M. A.; Gomez, J.; Lopez, M. L.; Pico, C.; Veiga, M. L. *Solid State Ionics.* **1997**, *95*, 241.
(12) Tarvin, R.; Davies, P. K. *J. Am. Ceram. Soc.* **2004**, *87*, 859.
(13) Arillo, A. M.; Gomez, J.; Lopez, M. L.; Pico, C.; Veiga, M. L. *J. Mater. Chem.* **1997**, *7*, 801.
(14) Knapp, M. C.; Woodward, P. M. *J. Solid State Chem.* **2006**, *179*, 1076.
(15) Ranjan, R.; Senyshyn, A.; Boysen, H.; Baehtz, C.; Frey, F. *J. Solid State Chem.* **2007**, *180*, 995.

10.1021/cm0716708 CCC: $37.00 © XXXX American Chemical Society
Published on Web 11/20/2007

Table 1. Results from Synthetic Attempts to Prepare New $AA'BWO_6$ Perovskites

A	*A′*	*B*	resulting phases	color	final annealing temperature (°C)	tolerance factor
Na	Nd	Mg	$NaNdMgWO_6$	light blue	1050	0.91
K	La	Mn	$KLaMnWO_6$	dark yellow	1000	0.97
K	Nd	Mn	K_2WO_4 + MnO + Nd_2WO_6		1050	0.96
Na	La	Mn	$NaLaMnWO_6$	yellow	1000	0.93
Na	Nd	Mn	$NaNdMnWO_6$	yellow	1000	0.91
Na	Tb	Mn	$NaTbMnWO_6$	green	950	0.91
Na	Y	Mn	Na_2WO_4 + MnO + others		1050	0.90
Na	Nd	Co	$NaNdCoWO_6$	brown	975	0.94
K	La	Ni	unidentified products		1200	1.00
Na	Nd	Ni	Na_2WO_4 + others		1050	0.94
Na	La	Cu	Na_2WO_4 + others		950	0.95
Na	La	Zn	Na_2WO_4 + others		1050	0.95

stood.[14] It was shown that layered ordering of *A* and *A′* cations leads to a bonding instability that is ameliorated by second-order Jahn–Teller (SOJT) distortions of cations populating the *B′*-sites. Thus, layered ordering of *A*-site cations is favored when the *B′* cation is a highly charged d^0 cation. Building upon this idea, we have used rational design concepts to prepare a series of new $AA'BB'O_6$ perovskites possessing simultaneous *A*- and *B*-site cation ordering, effectively doubling the size of this family. In particular, the presence of both SOJT distortions of d^0 cations and magnetic ions makes this family of compounds potentially attractive candidates for multiferroic behavior. In this paper we present the structures, magnetic properties, and electronic properties of six new $AA'BWO_6$ quintinary perovskites exhibiting simultaneous *A*- and *B*-site ordering.

Experimental Section

All compounds were synthesized using conventional ceramic methods. Starting materials for the reactions were reagent grade: Na_2CO_3 (Fisher 99.9%), K_2CO_3 (Baker 99.9%), La_2O_3 (G. Frederick Smith 99.99%), Y_2O_3 (Cerac 99.999%), Nd_2O_3 (Lindsay 99%), Tb_4O_7 (Cerac 99.9%), $NiWO_4$ (Alfa Aesar 99.9%), MnO (Cerac 99.9%), $CoCO_3$ (Johnson Matthey 99%), ZnO (Alfa Aesar 99.99%), $CuCO_3$ (99.9%), and WO_3 (Cerac 99.99%). Synthesis was aided by the use of BWO_4 ternary oxides as precursors. $MnWO_4$, $CoWO_4$, and $ZnWO_4$ were prepared from their respective binary oxides using ceramic methods while $NiWO_4$ was purchased and used as received. When Cu was used as the divalent cation, $CuCO_3$ and WO_3 were used directly. Stoichiometric amounts of the reactants were ground together and heated in a high-temperature furnace. A 5% excess of the alkali metal carbonates, Na_2CO_3 or K_2CO_3, were used to account for the high-temperature volatility of these substances.

$NaNdCoWO_6$ and $NaNdMgWO_6$ could be prepared by heating in air. $KLaMnWO_6$, $NaLaMnWO_6$, $NaNdMnWO_6$, and $NaTbMnWO_6$ were prepared by first heating to 800 °C in air and then to a higher final temperature under a dynamic flow of forming gas (5% H_2, 95% N_2). Attempts to prepare $AA'MnWO_6$ samples in air did not lead to the formation of a perovskite product. This failure is presumably linked to the redox chemistry of manganese. Final annealing temperatures for all compounds ranged from 950 to 1200 °C. Exact values are listed in Table 1.

X-ray powder diffraction patterns were collected on a Bruker D8 diffractometer (40 kV, 50 mA, Cu $K\alpha_1$ radiation) equipped with a Ge 111 incident beam monochromator and a Braun linear position-sensitive detector. Scans were recorded over a 2θ range of 8°–100°. A step size of either 0.014 286° 2θ or 0.007 168° 2θ was used, and the counting time was 2–2.5 s/step. Structure refinements of X-ray data were carried out using the Rietveld method as implemented in the TOPAS Academic[16] software package. Soft oxygen–oxygen distance constraints were use in most cases to promote convergence to the global minimum.

Neutron powder diffraction data were collected using the BT-1 32 detector neutron powder diffractometer at the NIST Center for Neutron Research (NCNR). A Cu(311) monochromator with a 90° takeoff angle, $\lambda = 1.5403(2)$ Å, and in-pile collimation of 15 min of arc were used. Data were collected over the range of 3–168° 2θ with a step size of 0.05°. The instrument is described in the NCNR Web site (http://www.ncnr.nist.gov/). Structure refinements of neutron data were performed using the GSAS[17,18] software package. Soft constraints were not used in the analysis of the neutron diffraction data.

UV–vis diffuse reflectance spectra were taken on Perkin-Elmer Lambda 20 spectrometer equipped with a 50 mm integrating sphere (Labsphere). Scans were done in 1 nm increments from 200 to 1000 nm at a scan rate of 30 nm/min. Magnetic susceptibility vs temperature measurements were taken on a Quantum Design MPMS 5XL SQUID magnetometer in the temperature range 2–400 K with a field strength of 1.00×10^3 Oe. Although zero-field-cooled and field-cooled data were collected, there are no significant differences between the two. Hence, only the zero-field-cooled data are reported.

Results and Discussion

Synthesis. In the course of this work six new fully ordered $AA'BWO_6$ perovskites have been obtained. Attempts at forming perovskite phases with additional compositions were also undertaken. Table 1 lists the results obtained using various combinations of cations along with the tolerance factors of the target perovskite phases. Of the six samples, five appeared to be phase pure. The XRD pattern of $NaNdMgWO_6$ had a small peak that could not be fit and is presumed to be due to a small amount of an impurity. Additional heating cycles were unsuccessful at eliminating this impurity.

Before discussing the structures and properties of the new phases, it is informative to look at those compositions where the synthesis was unsuccessful. A common feature to most of the unsuccessful synthesis attempts is the formation of A_2WO_4 ($A = Na^+, K^+$) in preference to formation of a

(16) *Topas Academic, General Profile and Structure Analysis Software for Powder Diffraction Data*; Bruker AXS: Karlsruhe, Germany, 2004.
(17) Toby, B. H. EXPGUI, a graphical user interface for GSAS. *J. Appl. Crystallogr.* **2001**, *34*, 210–21.
(18) Larson. A. C.; Von Dreele, R. B. General Structure Analysis System (GSAS), Los Alamos National Laboratory Report LAUR 86-748, 2004.

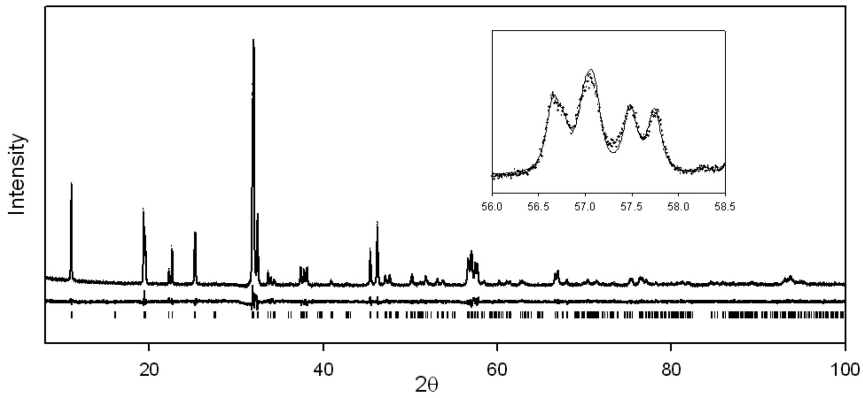

Figure 1. Powder XRD pattern of $NaNdMnWO_6$ showing observed (dotted line), calculated (solid line), and difference (beneath) curves. The expected peak positions are marked with vertical tick marks. The XRD patterns of the other compounds reported here are similar in appearance and can be found in the Supporting Information.

perovskite phase. Because the coordination numbers of both tungsten and the alkali metal cation increase upon going from A_2WO_4 to perovskite, it is possible that high-pressure synthesis routes may succeed in cases where ambient-pressure synthesis attempts did not.

Clearly there are a number of factors that play a role in determining the stability of the perovskite phase, including the size mismatch between alkali metal cation and rare earth cation, the tolerance factor, and the preferred oxidation state and coordination environment of the *B*-site cation. The fact that both $KLaMnWO_6$ and $NaNdMnWO_6$ could be formed, whereas $KNdMnWO_6$ could not, suggests a destabilization of this structure as the size difference between *A* and *A′* cations increases. There also appears to be a subtle destabilization as the covalency of the *B*–O bonding increases. For example, $NaLaBWO_6$ can be formed when $B = Mg^{2+}$, Mn^{2+}, Co^{2+}, and Ni^{2+}, but not when $B = Cu^{2+}$ or Zn^{2+}. Of course, it is possible that the instability of the latter two compounds stems from the Jahn–Teller distortion that accompanies Cu^{2+} and the tendency for Zn^{2+} to adopt tetrahedral coordination. However, a similar trend is seen in $NaNdBWO_6$ compositions where the $AA'BWO_6$ perovskite phase is formed when $B = Mg^{2+}$, Mn^{2+}, and Co^{2+} but not when $B = Ni^{2+}$. In this case the octahedral environment of the ordered perovskite structure is well matched to the coordination preferences of the Ni^{2+} ion.

The colors of the $AA'MnWO_6$ samples varied somewhat depending on the synthesis temperature. When synthesized at 900 °C they appear green, but when synthesized at 1000 °C or higher they appear yellow. When synthesized at 950 °C they are a greenish-yellow or orange. The powder XRD patterns of these different forms are indistinguishable. The green coloration of the samples prepared at lower temperature is thought to arise from a slight oxidation of the samples, which should lead to the presence of Mn^{3+}. From the data available it is not possible to know the nature of the defects, although it is possible that the green samples have a slight oxygen excess (manifest through cation vacancies). UV–vis measurements of green and yellow samples of $NaLaMnWO_6$ gave similar spectra with one exception. The green sample has an additional absorbance at wavelengths below the band gap in the red and IR regions. This suggests that the yellow

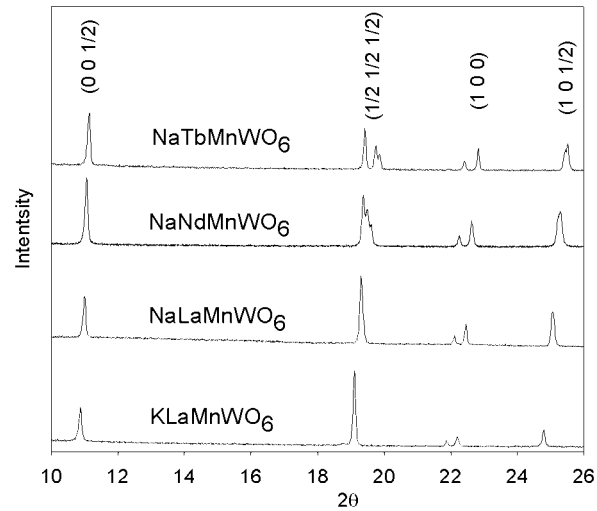

Figure 2. Powder XRD patterns of the four $AA'MnWO_6$ compounds. The pseudocubic ($^1/_2$ $^1/_2$ $^1/_2$) group of reflections is indicative of rock-salt ordering of Mn and W cations, while the (0 0 $^1/_2$) and (1 0 $^1/_2$) groups of reflections are indicative of layered ordering of the *A* and *A′* cations.

samples are closer to the ideal stoichiometry. All subsequent characterizations were carried out on the yellow samples.

X-ray Powder Diffraction. Monochromatic X-ray powder diffraction data were used to structurally characterize all samples. Rietveld refinements were carried out to confirm the structure, determine lattice parameters, and estimate the *A*- and *B*-site cation ordering. In addition to the expected perovskite subcell reflections, supercell reflections resulting from cation ordering are observed in all cases. The presence of strong reflections with pseudo-cubic indices ($^1/_2$ $^1/_2$ $^1/_2$) and (1 $^1/_2$ $^1/_2$), as indexed on the primitive cubic perovskite subcell, are indicative of rock salt ordering of the *B*-site cations. The presence of strong peaks at ($^1/_2$ 0 0) and (0 1 $^1/_2$) are indicative of layered ordering of the *A*-site cations (Figures 1 and 2). The refinements show that in all cases the *B*-site order is complete, as would be expected when the oxidation states of the *B* and *B′* cations differ by four. The *A*-site order is complete or nearly complete in all samples as well. The long-range order parameter (LRO) for *A*-site ordering is given in Table 2. The refinements also confirm the displacement of W^{6+} ions toward the layer containing monovalent *A*-site cations. This displacement is driven by a

Table 2. Crystallographic and Electronic Data on the $AA'BB'O_6$ Compounds as Obtained from X-ray Powder Diffraction and UV–vis Diffuse Reflectance Spectroscopy

compound	a (Å)	b (Å)	c (Å)	β (deg)	V/Z	A-site LRO (%)[a]	band gap (eV)
$KLaMnWO_6$	5.6537(0)		8.1109(1)		129.63(0)	87.5(5)	2.2
$NaLaMnWO_6$	5.5857(1)	5.6026(1)	8.0313(1)	90.22(0)	125.67(1)	91.2(3)	2.4
$NaNdMnWO_6$	5.5101(1)	5.5948(1)	7.9861(1)	90.36(0)	123.09(1)	95.3(4)	2.3
$NaTbMnWO_6$	5.4228(1)	5.5822(1)	7.9220(1)	89.65(0)	119.90(1)	100.0(8)	2.2
$NaNdCoWO_6$	5.4788(2)	5.5098(2)	7.8533(3)	90.14(0)	118.53(1)	90.3(9)	2.6
$NaNdMgWO_6$	5.4789(2)	5.4848(2)	7.8566(3)	90.16(0)	118.05(1)	85.9(5)	4.0

[a] The LRO order parameter is a percentage calculated from the occupancy of the Na(La) ion on its crystallographic site, S_A. The LRO parameter is equal to $2S_A - 1$. Defined in this way, the LRO parameter varies from 100% when the Na(K) and Ln ions are perfectly ordered ($S_A = 1.0$) to 0% when Na(K) and the Ln ions are randomly distributed ($S_A = 0.50$). Constraints were imposed that maintain full occupation of the Na(K) and Ln sites as well as the overall stoichiometry of the sample.

second-order Jahn–Teller distortion of the W^{6+} cation and is thought to be necessary for stabilizing the layered ordering of the A-site cations.[14]

The X-ray diffraction patterns of all six compounds could be successfully fit using a $\sqrt{2}a_p \times \sqrt{2}a_p \times 2a_p$ unit cell, where a_p is the length of the unit cell in the cubic ABX_3 perovskite structure ($a_p \cong 4$ Å). Not surprisingly, as the tolerance factor decreases the difference between the a and b lattice parameters increases as does the degree of peak splitting. This is the behavior that would be expected if the octahedral tilting distortion increases as the tolerance factor is lowered. All visible reflections in the pattern of $KLaMnWO_6$ could be accounted for using the space group $P4/nmm$ (129). This space group does not allow for any rotation of the octahedra. The fit obtained using this model was good and agreed closely with the Pawley fit. The use of lower symmetry space groups did not significantly improve the fit.

The XRD patterns of all other compounds showed some degree of peak splitting, as seen in Figures 1 and 2, which necessitated the use of a monoclinic variant of the unit cell. The possible monoclinic unit cells could have dimensions of $\sqrt{2}a_p \times \sqrt{2}a_p \times 2a_p$ or $2a_p \times 2a_p \times 2a_p$. For $NaLaMnWO_6$, $NaNdCoWO_6$, and $NaNdMgWO_6$ it is possible to index the peaks with either unit cell, but the use of a $\sqrt{2}a_p \times \sqrt{2}a_p \times 2a_p$ provided a superior fit in the refinement stage. For $NaNdMnWO_6$ and $NaTbMnWO_6$ the observed peak splitting could only be indexed using a $\sqrt{2}a_p \times \sqrt{2}a_p \times 2a_p$ unit cell, thereby eliminating any ambiguity. On the basis of the previously published group theoretical analysis of distorted $AA'BB'O_6$ perovskites, this monoclinic unit cell is consistent with two possible octahedral tilting distortions of the structure.[14] Out-of-phase rotations of the octahedra about the [110] direction of the cubic structure (tilt system $a^-a^-c^0$ using Glazer notation)[19] leads to $P2_1/m$ (#11) symmetry. If an additional in-phase rotation of the octahedra occurs about the c-axis (tilt system $a^-a^-c^+$ using Glazer notation),[19] the symmetry is further lowered to $P2_1$ (#4). The presence of an additional tilt is significant because it destroys the inversion center, allowing for the formation of a polar structure, which is an important consideration for multiferroic applications that provide the motivation for this work.

Because the $P2_1/m$ and $P2_1$ structures have identical extinction conditions, the distinction between the two comes down to differences in peak intensities. The X-ray diffraction patterns of $NaLaMnWO_6$ and $NaNdMgWO_6$ could be fit quite well using the $P2_1/m$ (#11) model, while the fit to the $NaNdMnWO_6$, $NaTbMnWO_6$, and $NaNdCoWO_6$ patterns improved noticeably when the space group symmetry was lowered to $P2_1$ (#4). However, because they differ structurally only in the rotation of the oxygen octahedra about the c-axis, it is difficult to definitively differentiate between these two possibilities on the basis of X-ray data alone. The neutron diffraction results discussed in the following section provide a more conclusive picture.

Neutron Powder Diffraction. Neutron powder diffraction data were collected in order to better determine the arrangement of the anion sublattice. This was essential for assignment of a space group. For $NaTbMnWO_6$ and $NaNdMnWO_6$ Rietveld refinements using a $P2_1/m$ model were not able to accurately account for the peak intensities, whereas fits using a $P2_1$ model provided good fits, thereby confirming $P2_1$ symmetry. Somewhat surprisingly, given the analysis of the X-ray diffraction data, a $P2_1$ model provided a superior fit the neutron diffraction pattern of $NaLaMnWO_6$ as well, showing that this compound also possesses an in-phase tilt about the c-axis. A bond valence sum analysis yields reasonable values for all ions in each of the three compounds. The NPD patterns and their fits are shown in Figure 3. Further details are given in the Supporting Information. Selected bond lengths, bond angles, and bond valence sums are given in Table 3. Full structural parameters are given in the Supporting Information.

A second-order Jahn–Teller distortion of the B' cation has been proposed to be responsible for the stabilization of layered A-site cation ordering in these perovskites. Now that reliable crystal structures have been obtained, we have further investigated the distortion of the W^{6+} ion on the B-site. The program IVTON[20] was used to calculate the displacements of the B-site cations from the centers of their octahedra. The results show that the W^{6+} ion is significantly distorted in all three cases (Table 4). Investigation of the direction of the displacement reveals that the tungsten is distorted primarily along the c-axis and toward the Na^+ layer, as expected. The combination of this distortion and a large tilting of the octahedra leads to three short and three long W–O bonds. The bond valence sums show that the coupling between tilting and cation displacement is such that all six crystallographically distinct oxygens are able to find suitable environments.

(19) Glazer, A. M. *Acta Crystallogr., Sect. B: Struct. Sci.* **1972**, *28*, 3384.

(20) Balic Zunic, T.; Vickovic, I. *J. Appl. Crystallogr.* **1996**, *29*, 305.

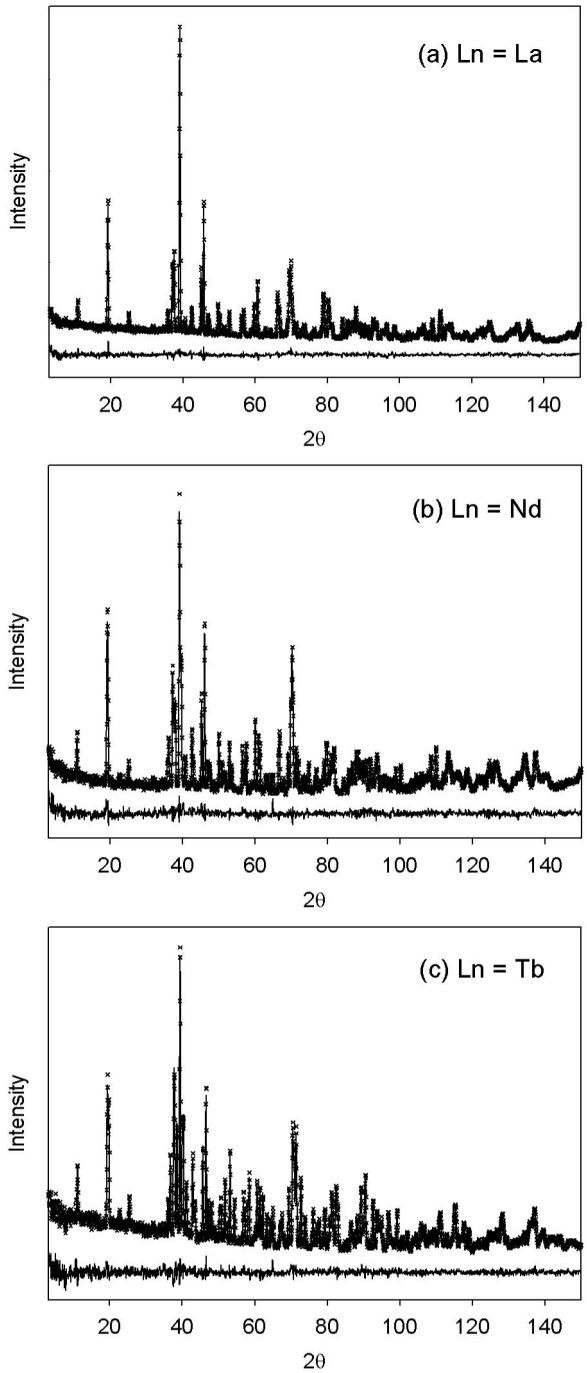

Figure 3. Neutron powder diffraction patterns for some Na*Ln*MnWO$_6$ compounds at room temperature showing observed (dotted line), calculated (solid line), and difference (beneath) curves.

The neutron diffraction patterns of KLaMnWO$_6$, NaNdMgWO$_6$, and NaNdCoWO$_6$ all have additional peaks that cannot be indexed using any space group that only accounts for cation ordering and simple in-phase or out-of-phase octahedral tilting. Similar satellite peaks have been reported in the NPD patterns of NaLaMgWO$_6$, KLaMgWO$_6$, and NaLaScNbO$_6$.[21] The fact that these peaks were not evident in the XRD patterns suggests that they are associated with the atomic positions of the oxygen ions. We speculate that a complex octahedral tilting pattern may be responsible.

(21) Knapp, M. C. Ph.D. Thesis, The Ohio State University, 2006.

Table 3. Select Bond Distances and Angles as Well as Bond Valence Sums

	NaLaMnWO$_6$	NaNdMnWO$_6$	NaTbMnWO$_6$
bond distances			
Mn–O(1)	2.212(14)	2.208(15)	2.252(10)
Mn–O(2)	2.162(15)	2.171(16)	2.126(10)
Mn–O(3)	2.135(15)	2.130(16)	2.190(10)
Mn–O(4)	2.111(14)	2.134(16)	2.109(10)
Mn–O(5)	2.224(11)	2.206(14)	2.176(9)
Mn–O(6)	2.109(11)	2.110(14)	2.130(9)
Mn–O average	2.159	2.160	2.164
W–O(1)	1.969(12)	1.969(10)	1.954(8)
W–O(2)	2.002(12)	1.967(10)	1.999(8)
W–O(3)	1.820(12)	1.887(11)	1.845(8)
W–O(4)	1.878(13)	1.856(11)	1.888(8)
W–O(5)	2.083(8)	2.086(10)	2.100(7)
W–O(6)	1.825(8)	1.821(10)	1.816(7)
W–O average	1.930	1.931	1.934
bond valence sums			
Ln	3.132	3.063	2.992
Na	0.943	1.054	1.161
Mn	2.232	2.220	2.203
W	5.994	5.937	5.929
O(1)	2.044	1.974	1.958
O(2)	2.009	2.059	2.028
O(3)	2.160	2.025	2.094
O(4)	2.045	2.121	2.054
O(5)	1.953	1.988	1.976
O(6)	2.090	2.107	2.175
bond angles			
Mn–O(1)–W	148.19(55)	144.68(53)	142.49(38)
Mn–O(2)–W	148.84(57)	143.95(56)	141.30(40)
Mn–O(3)–W	161.17(59)	154.17(60)	149.63(41)
Mn–O(4)–W	154.60(60)	151.69(63)	144.02(41)
Mn–O(5)–W	157.99(40)	153.28(50)	147.89(36)
Mn–O(6)–W	150.41(44)	151.24(57)	150.53(39)

Table 4. Displacements (Å) of the Mn and W Atoms from the Centers of Their Octahedra and the *x*, *y*, and *z* Components of the Displacement Vector for the W Atom

	NaLaMnWO$_6$	NaNdMnWO$_6$	NaTbMnWO$_6$
Mn displacement	0.076	0.063	0.081
W displacement	0.163	0.148	0.162
x vector	0.067	0.029	0.042
y vector	0.025	−0.017	0.024
z vector	0.146	0.145	0.156

Further analysis is required to determine the crystallographic origins of these effects. Such work is currently in progress.

Electronic Structure. Diffuse reflectance spectra are shown in Figure 5. There are a number of electronic excitations that can take place in these oxides. Localized intra-atomic excitations can occur. These could be either d-to-d transitions centered on the Mn^{2+} or Co^{2+} ions, or they could be f-to-f transitions centered on Nd^{3+} or Tb^{3+}. Band-to-band transitions with a significant charge-transfer character are also possible. To assign the features in the optical spectra to specific electronic transitions, let us begin with NaNdMgWO$_6$, shown in the lower part of Figure 5. Localized transitions involving the Mg^{2+} can be ruled out. Therefore, the relatively sharp peaks observed at ~590, 747, 808, and 880 nm can be assigned to localized f-to-f transitions associated with Nd^{3+} ions. The strongest localized excitation falls in the orange region of the spectrum and is responsible for the light blue color of this compound. The strong upturn in absorbance that occurs in the UV region is associated with excitations from the O 2p valence band into the antibonding W 5d–O 2p conduction band. The band gap of 4.0 eV is slightly larger, but of the same order of

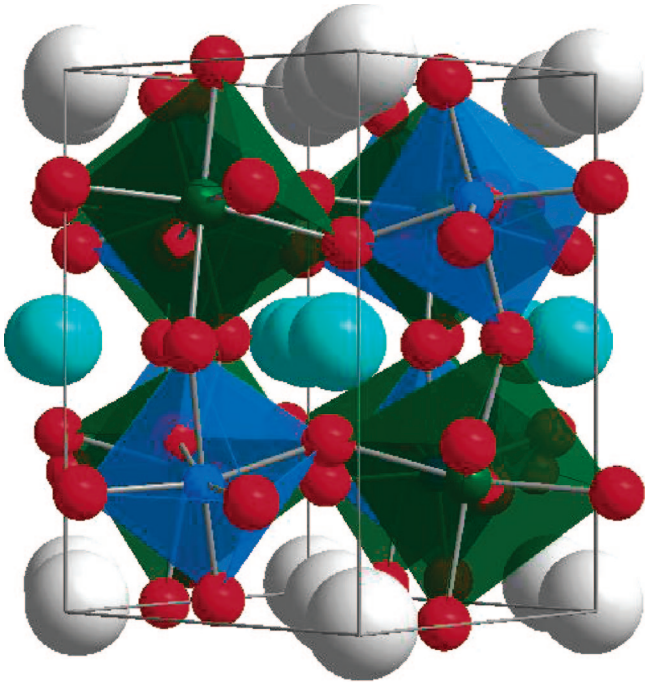

Figure 4. Crystal structure of $NaTbMnWO_6$. The small spheres are W^{6+} (blue), Mn^{2+} (green), and O^{2-} (red). Large spheres are Na^+ (light gray) and Nd^{3+} (aqua).

magnitude, as the reported band gaps of related double perovskites Sr_2MgWO_6 (3.6 eV) and Ba_2MgWO_6 (3.4 eV).[22]

Upon replacing Mg^{2+} with Mn^{2+}, a significant red shift of the band gap results. However, new peaks that can be assigned to localized transitions are not observed. The absence of peaks associated with d-to-d transitions on the Mn^{2+} ion is perhaps not surprising considering the fact that all such transitions are spin-forbidden. The band gap energies can be estimated by extrapolating the linear portion of the absorption to zero absorbance. These values are reported in Table 2. The band gap value is reduced from 4.0 eV in $NaNdMgWO_6$ to 2.2–2.4 eV in the $AA'MnWO_6$ samples. There are several factors that play a role in the large reduction of the band gap. The simplest description would be one where localized electrons populating the d-orbitals on manganese are excited into the empty W 5d–O 2p conduction band. The energy levels of the Mn 3d orbitals will undoubtedly fall at a higher energy than the nonbonding O 2p band that is common to all perovskites in this family. This description emphasizes a localized picture of the bonding. In reality, there will be some mixing of Mn 3d, O 2p, and W 5d orbitals to form extended bands.

The optical spectrum of $NaNdCoWO_6$ is quite similar to that of $NaNdMnWO_6$. However, despite its larger band gap, $NaNdCoWO_6$ absorbs more strongly at energies below the band gap. The extra absorption of this compound is most likely due to d-to-d transitions associated with the Co^{2+} ion. These absorptions can now be observed because they are no longer spin forbidden. Octahedrally coordinated Co^{2+} oxides typically absorb at around 510 and 580 nm,[23] which is consistent with observation of increased absorbance in this region.

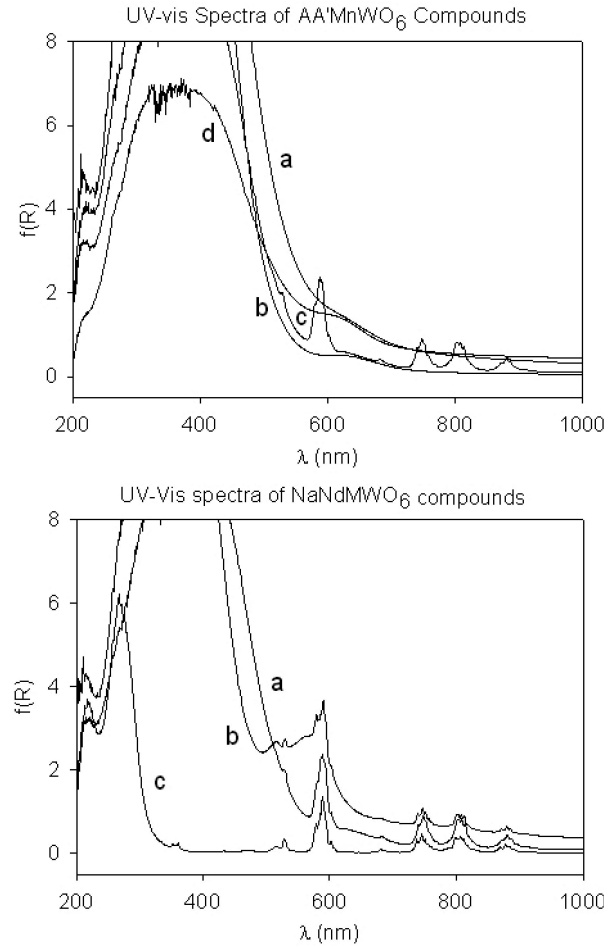

Figure 5. UV–vis diffuse reflectance spectra. The top plot shows the spectra for (a) $KLaMnWO_6$, (b) $NaLaMnWO_6$, (c) $NaNdMnWO_6$, and (d) $NaTbMnWO_6$. The bottom plot shows the spectra for (a) $NaNdMnWO_6$, (b) $NaNdCoWO_6$, and (c) $NaNdMgWO_6$.

Magnetic Properties. Magnetic susceptibility vs temperature measurements were made on the four $AA'MnWO_6$ compounds. The results show all four samples to be low-temperature antiferromagnets with Néel temperatures ranging from 6 to 15 K. Curie–Weiss plots were constructed for all four samples by plotting $1/\chi_m$ vs T over the paramagnetic temperature range (Figure 6). From these plots the Curie constant (C) and the Weiss constant (Θ) were obtained (see Table 5). The temperature range of 120–300 K provided the best linear fit to the data and was used to extract these values. The high-spin d^5 configuration of the Mn^{2+} ion is such that the magnetic moment is rigorously equal to the spin-only contribution to the magnetic moment (the orbital angular momentum is zero). The magnetic moment of the Mn^{2+} can therefore be calculated to be 5.92 μ_B with the formula $\mu = g(S(S+1))^{1/2}$, where $g = 2.0023$ and $S = 5/2$.

The μ_{eff} of the $KLaMnWO_6$ and $NaLaMnWO_6$ samples were 5.785 and 5.911 μ_B, respectively. The agreement between the effective and expected magnetic moments for

(22) Eng, H. W.; Barnes, P. W.; Auer, B. M.; Woodward, P. M. *J. Solid State Chem.* **2003**, *175*, 94.

(23) Duffy, J. A. *Bonding, Energy Levels and Bands in Inorganic Solids*; John Wiley & Sons: New York, 1990; p 51.

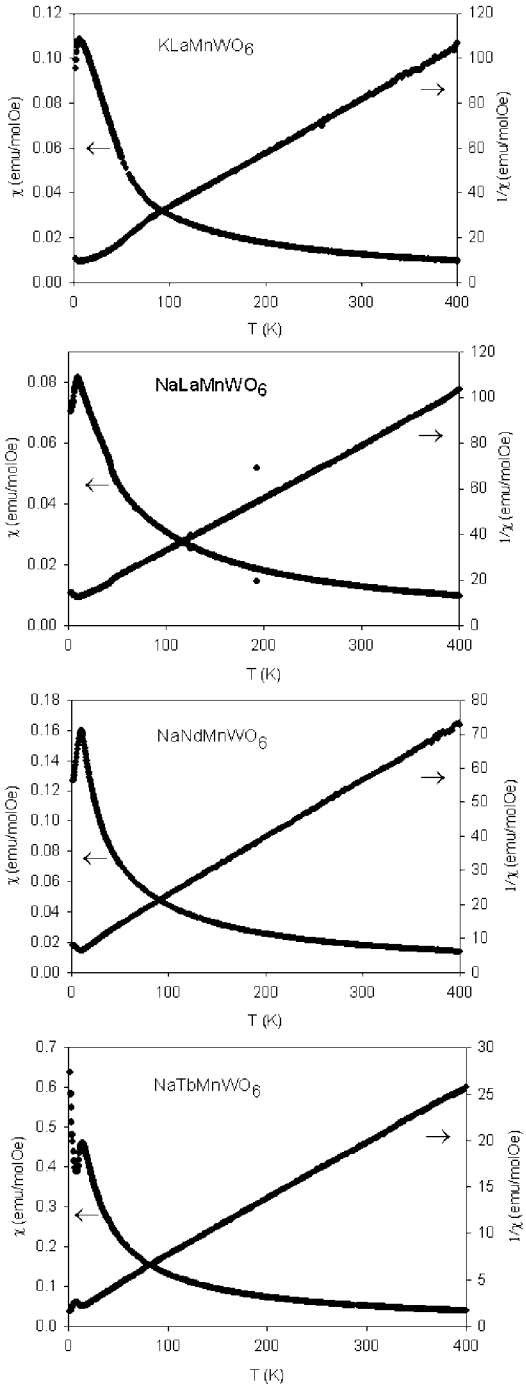

Figure 6. Magnetic susceptibility measurements for KLaMnWO$_6$, NaLaMnWO$_6$, NaNdMnWO$_6$, and NaTbMnWO$_6$. Plots of magnetic susceptibility χ vs temperature are shown on the left *y*-axis, while $1/\chi$ vs temperature is plotted on the right *y*-axis.

Table 5. Magnetic Data for the *AA′*MnWO$_6$ Compounds

compound	T_N (K)	*C* (emu K/ mol Oe)	Θ (K)	μ_{eff}/μ_B	μ_{theory}/μ_B
KLaMnWO$_6$	6	4.184(4)	−40.10(8)	5.785(4)	5.916
NaLaMnWO$_6$	10	4.369(3)	−42.25(6)	5.911(3)	5.916
NaNdMnWO$_6$	11	5.938(2)	−35.43(5)	6.891(2)	6.936
NaTbMnWO$_6$	15	16.52(1)	−27.29(1)	11.49(1)	11.38

NaLaMnWO$_6$ is excellent, confirming the high-spin configuration and +2 oxidation state of the manganese ion. The agreement for KLaMnWO$_6$ is not quite as good, but there is almost no doubt that the predominant magnetic ion in this phase is also high-spin Mn^{2+}. The theoretical moments of the lanthanides were calculated by taking into account spin–orbit coupling. For the two samples containing magnetic lanthanides the theoretical total moment per formula unit was calculated by using the formula $(\mu_{total})^2 = (\mu_{Ln})^2 + (\mu_{Mn})^2$. Once again, the values obtained agree well with the experimental values.

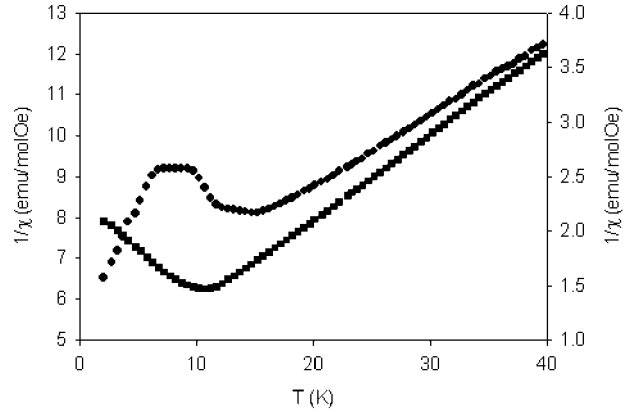

Figure 7. A magnification of the low-temperature region of the $1/\chi$ vs temperature plot for NaNdMnWO$_6$ (left *y*-axis, squares) and NaTbMnWO$_6$ (right *y*-axis, circles).

In addition to the single antiferromagnetic transition that the other three samples exhibit, the NaTbMnWO$_6$ sample also shows a second transition at 9 K where the susceptibility begins to increase once again (Figure 7). This behavior suggests a sequence of phase transitions resulting from coupling between the Mn^{2+} magnetic sublattice and the Tb^{3+} magnetic sublattice. Interestingly the NaNdMnWO$_6$ sample, which also contains a magnetic cation on the *A*-site, does not show this behavior. Similar behavior is seen in multiferroic oxides such as TbMnO$_3$[24] and TbMn$_2$O$_5$.[25] The preliminary results of low-temperature neutron diffraction studies are shown in Figure 8. They confirm the presence of at least two magnetic phase transitions in NaTbMnWO$_6$.

The neutron diffraction pattern of NaLaMnWO$_6$ changes upon cooling through T_N. The low-temperature pattern is very similar to the neutron diffraction pattern previously published for Ba$_2$MnWO$_6$,[26] indicating that antiferromagnetic Mn–O–W–O–Mn superexchange interactions are dominant. The neutron diffraction pattern of NaNdMnWO$_6$ taken below T_N is noticeably different. The most plausible explanation for this is that the Nd^{3+} ions also participate in the magnetic ordering. NaTbMnWO$_6$ shows an even more interesting behavior. Upon going through the higher temperature transition, it adopts a complicated magnetic unit cell that appears to be similar to NaNdMnWO$_6$, then upon cooling to 6 K the magnetic structure adopts the same unit cell as does NaLaMnWO$_6$ at 5 K, but the peak intensities are quite different, which strongly implies ordering of the Tb^{3+} ions. Full details of the magnetic phase transitions as well as studies of magnetoelectric coupling will be published later.

(24) Kajimoto, R.; Yoshizawa, H.; Shintani, H.; Kimura, T.; Tokura, Y. *Condens. Matter* **2004**, 1–5.
(25) Hur, N.; Park, S.; Sharma, P. A.; Ahn, J. S.; Guha, S.; Cheong, S.-W. *Nature (London)* **2004**, *429*, 392.
(26) Azad, A. K.; Ivanov, S. A.; Eriksson, S.-G.; Eriksen, J.; Rundlof, H.; Mathieu, R.; Svedlindh, P. *Mater. Res. Bull.* **2001**, *36*, 2215–2228.

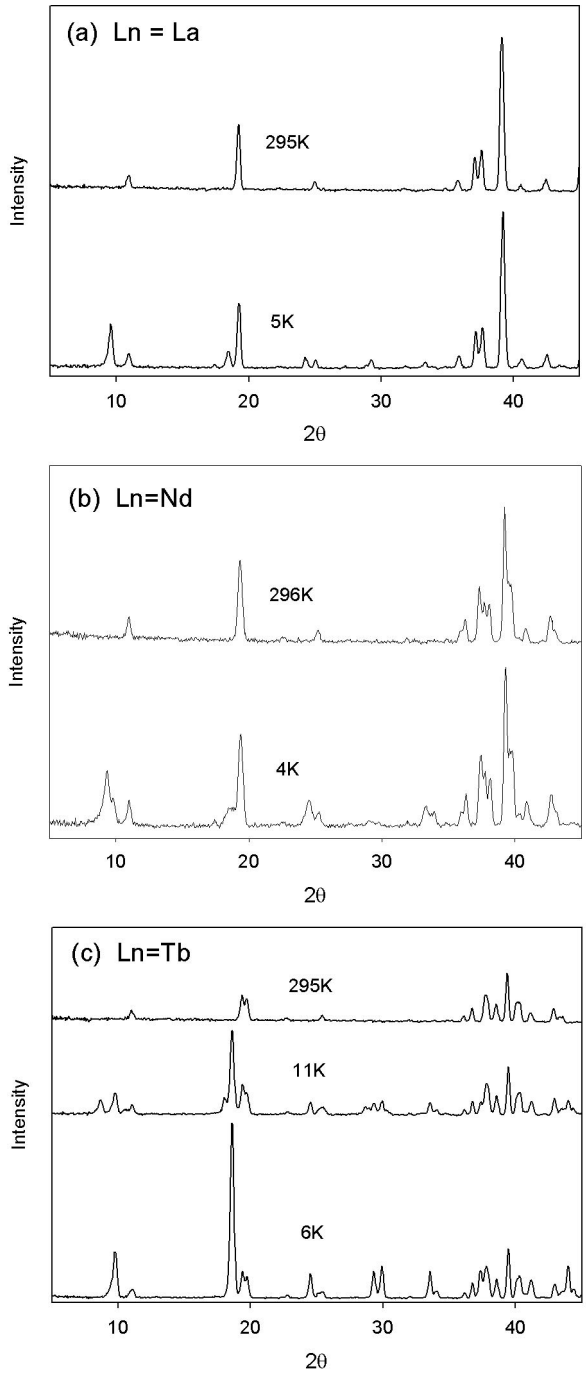

Figure 8. Neutron powder diffraction patterns of Na*Ln*$MnWO_6$ compounds at a series of temperatures showing the evolution of the magnetic peaks.

The low Néel temperatures can be attributed to the large spacing between the magnetic Mn^{2+} ions. Superexchange interactions which are responsible for the magnetic ordering must propagate through four bonds, Mn–O–W–O–Mn, to stabilize the ordered structure. As we see in Table 5, the Néel temperature increases as the average size of the *A*-site cations decreases. In contrast, the Weiss constant decreases in magnitude across the same set of compounds. The decreasing Weiss constant can be rationalized in terms of orbital overlap. As the tolerance factor decreases, the linearity of the Mn–O–W–O–Mn chains also decreases. This reduces orbital overlap, and therefore the Weiss constant, which is dependent upon the strength of the exchange interaction, decreases.

If the strength of the magnetic exchange interactions decrease as the tolerance factors decreases, why does the Néel temperature increase? It is well-known in ordered perovskites that linear Mn–O–W–O–Mn superexchange interactions compete with 90° Mn–O–O–Mn interactions across the face of the unit cell. If the latter type of coupling is dominant, each Mn^{2+} ion is tetrahedrally coordinated to its nearest interacting Mn^{2+} magnetic neighbors, which is a situation that leads to magnetic frustration. Octahedral tilting helps to relieve this frustration, thereby increasing the Néel temperature. A similar trend has been observed in another series of $AA'MnWO_6$ compounds (AA' = Ba_2, BaSr, Sr_2, SrCa, Ca_2) in which the Néel temperature increases from 9 to 16 K as the average size of the *A*-cations decreased.[27]

Conclusions

The perovskites $KLaMnWO_6$, $NaLaMnWO_6$, $NaNdMnWO_6$, $NaTbMnWO_6$, $NaNdCoWO_6$, and $NaNdMgWO_6$ have been synthesized and characterized for the first time. This work extends the family of complex perovskites with layered ordering of the *A*-site cations and rock-salt ordering of the *B*-site cations. $NaNdMgWO_6$ is an insulator with a band gap of ~4.0 eV, while the other compounds are semiconductors with band gaps in the range 2.2–2.4 eV. The $AA'MnWO_6$ samples show a paramagnetic to antiferromagnetic transition with Néel temperatures ranging from 6 to 15 K. The magnetic structure of $NaLaMnWO_6$ phase appears to be stabilized by antiferromagnetic Mn–O–W–O–Mn superexchange interactions, similar to related compounds like Ba_2MnWO_6. $NaNdMnWO_6$ adopts a more complicated magnetic structure. $NaTbMnWO_6$ undergoes two magnetic transitions at 15 and ~9 K. The more complex mangnetic behavior of the Nd and Tb analogues is thought to arise from coupling between the Mn^{2+} sublattice and the Nd^{3+}/Tb^{3+} sublattice.

Acknowledgment. Financial support from the NSF through a Materials World Network grant (MWN-0603128) and the NSF funded Center for the Design of Materials (CHE-0434567) is gratefully acknowledged. We also thank Ram Seshadri and the UCSB MRL MRSEC (NSF-DMR 0520415) for use of the SQUID facilities. We acknowledge the support of the National Institute of Standards and Technology, U.S. Department of Commerce, in providing the neutron research facilities used in this work. We thank Dr. Judith Stalick for assistance with the neutron diffraction experiments.

Supporting Information Available: Full XRD patterns of all samples and additional details regarding the refinements; individual NPD patterns of the three samples whose structures are reported and details regarding the refinements; structural parameters extracted from the neutron diffraction refinements. This material is available free of charge via the Internet at http://pubs.acs.org.

CM0716708

(27) Azad, A. K.; Eriksson, S.-G.; Ivanov, S. A.; Rundlof, H.; Eriksen, J.; Mathieu, R.; Svedlindh, P. *Ferroelectrics* **2002**, *269*, 105.